

# Global upper-mantle tomography with the automated multimode inversion of surface and $S$ -wave forms

Sergei Lebedev<sup>1</sup> and Rob D. van der Hilst<sup>1,2</sup>

<sup>1</sup>Utrecht University, Department of Earth Sciences, Budapestlaan 4, Utrecht, 3584 CD, The Netherlands. E-mail: sergei@geo.uu.nl

<sup>2</sup>Massachusetts Institute of Technology, EAPS, Cambridge, MA 02139, USA

Accepted 2008 January 1. Received 2007 November 27; in original form 2006 July 26

## SUMMARY

We apply the Automated Multimode Inversion of surface and  $S$ -wave forms to a large global data set, verify the accuracy of the method and assumptions behind it, and compute an  $S_v$ -velocity model of the upper mantle (crust–660 km). The model is constrained with  $\sim 51\,000$  seismograms recorded at 368 permanent and temporary broadband seismic stations. Structure of the mantle and crust is constrained by waveform information both from the fundamental-mode Rayleigh waves (periods from 20 to 400 s) and from  $S$  and multiple  $S$  waves (higher modes). In order to enhance the validity of the path-average approximation, we implement the automated inversion of surface- and  $S$ -wave forms with a three-dimensional (3-D) reference model. Linear equations obtained from the processing of all the seismograms of the data set are inverted for seismic velocity variations also relative to a 3-D reference, in this study composed of a 3-D model of the crust and a one-dimensional (1-D), global-average depth profile in the mantle below. Waveform information is related to shear- and compressional-velocity structure within approximate waveform sensitivity areas. We use two global triangular grids of knots with approximately equal interknot spacing within each: a finely spaced grid for integration over sensitivity areas and a rougher-spaced one for the model parametrization. For the tomographic inversion we use LSQR with horizontal and vertical smoothing and norm damping. We invert for isotropic variations in  $S$ - and  $P$ -wave velocities but also allow for  $S$ -wave azimuthal anisotropy—in order to minimize errors due to possible mapping of anisotropy into isotropic heterogeneity. The lateral resolution of the resulting isotropic upper-mantle images is a few hundred kilometres, varying with data sampling.

We validate the imaging technique with a ‘spectral-element’ resolution test: inverting a published global synthetic data set computed with the spectral-element method using a laterally heterogeneous mantle model we are able to reconstruct the synthetic model accurately. This test confirms both the accuracy of the implementation of the method and the validity of the JWKB and path-average approximations as applied in it.

Reviewing the tomographic model, we observe that low- $S_v$ -velocity anomalies beneath mid-ocean ridges and backarc basins extend down to  $\sim 100$  km depth only, shallower than according to some previous tomographic models; this presents a close match to published estimates of primary melt production depth ranges there. In the seismic lithosphere beneath cratons, unambiguous high velocity anomalies extend to  $\sim 200$  km. Pronounced low-velocity zones beneath cratonic lithosphere are rare; where present (South America; Tanzania) they are neighboured by volcanic areas near cratonic boundaries. The images of these low-velocity zones may indicate hot material—possibly of mantle-plume origin—trapped or spreading beneath the thick cratonic lithosphere.

**Key words:** Inverse theory; Numerical approximations and analysis; Mantle processes; Seismic tomography; Cratons; Dynamics of lithosphere and mantle.

## 1 INTRODUCTION

Resolution of global upper-mantle tomography has been improving in the last two decades thanks to the growth in the amount of high-

quality broadband data, the increase in computational power, and the development in data-processing techniques (e.g. Woodhouse & Dziewonski 1984; Zhang & Tanimoto 1993; Su *et al.* 1994; Masters *et al.* 1996, 2000; Megnin & Romanowicz 2000; Gu *et al.* 2001;

Shapiro & Ritzwoller 2002; Ritsema *et al.* 2004; Debayle *et al.* 2005; Zhou *et al.* 2006). Major upper-mantle features first imaged in early studies—including high-velocity anomalies beneath cratons and low-velocity anomalies beneath mid-ocean ridges and backarc basins—can now be mapped with a much greater accuracy, laterally and radially. The currently achievable resolution of a few hundred kilometres also begins to enable us to address a new class of questions pertaining to mantle dynamics on a relatively small scale of tectonic units (e.g. causes for regional variations in the structure of continental lithosphere; origin and implications of seismic anomalies beneath intraplate volcanic centres).

Multimode waveform techniques (Cara & L ev eque 1987; Nolet 1990; Gee & Jordan 1992) can constrain both the structure in the upper 200–300 km of the mantle—sampled primarily by the fundamental mode surface waves—and the structure below, down to the transition-zone—sampled by *S* and multiple *S* waves (e.g. Lebedev *et al.* 2002; Ritsema *et al.* 2004). They can yield more uniform resolution in the upper mantle compared both to teleseismic delay time tomography and to inversions of fundamental-mode surface-wave measurements, the former offering high upper-mantle resolution but only in regions with an abundance of seismic sources or stations (e.g. Bijwaard *et al.* 1998; K arason & van der Hilst 2000; Grand 2002), and the latter providing dense global sampling but mostly of structure in the upper half of the upper mantle (Trampert & Woodhouse 1995; Laske & Masters 1996; Ekstr om *et al.* 1997; Ritzwoller & Levshin 1998). The recently introduced Automated Multimode Inversion (AMI) of surface- and *S*-wave forms (Lebedev & Nolet 2003; Lebedev *et al.* 2005) enables the processing of very large amounts of data, selection of signal least likely to contain scattered waves, and balancing of the information extracted from waves of different amplitudes and different types. In this study, we develop the method further, apply it to a large global data set, and compute an upper-mantle model with a lateral resolution of a few hundred kilometres, varying laterally and radially with data sampling.

The method assumes the JWKB and path-average approximations (Dahlen & Tromp 1998) and the accuracy of the imaging depends on the validity of the approximations as applied in the data processing. AMI is able to select the time-frequency portions of the waveform signal that can be modelled accurately with the JWKB approximation (Lebedev *et al.* 2005). In order to enhance the validity of the path-average approximation, we now implement the technique with a 3-D reference model. Using the 3-D reference, we compute phase velocities of surface-wave modes and their derivatives as averages over approximate waveform sensitivity areas. Previously, 3-D reference models have been used in the inversion of phase- or group-velocity data (e.g. Boschi & Ekstr om 2002; Shapiro & Ritzwoller 2002) but not in a direct inversion of waveforms for seismic velocity structure. We also implement a fast and accurate scheme for setting up and solving the large linear inverse problem that results from processing tens or hundreds of thousand seismograms.

Validation of tomographic methods and models has long been difficult due to a fundamental problem: resolution tests have had to be performed using the same assumptions relating to wave propagation, in particular regarding structural sensitivity of seismic observables, as the inversion of the data. In this sense their results could always have been questioned as optimistic. Here we perform a resolution test of a new kind: we invert synthetic data computed by Qin *et al.* (2006) using the spectral-element method (Komatitsch *et al.* 2002; Capdeville *et al.* 2003) and a laterally heterogeneous mantle model. The advantage of this approach is that we are able to verify simultaneously the accuracy of the implementation of AMI

and the subsequent inversion and the validity of the approximations assumed.

Among the major features in the new tomographic model are the well-known high- $S_v$ -velocity anomalies beneath cratons and low- $S_v$ -velocity anomalies beneath mid-ocean ridges and backarc basins. Anomalies of both types extend shallower than inferred in many earlier studies (e.g. Woodhouse & Dziewonski 1984; Su *et al.* 1994; Zhou *et al.* 2006): down to  $\sim 200$  km for cratons—as also observed by Ritsema *et al.* (2004) and Debayle *et al.* (2005)—and down to  $\sim 100$  km for ridges and backarcs—as was also observed by Zhang & Tanimoto (1993) and, more recently, by Shapiro & Ritzwoller (2002) and Debayle *et al.* (2005).

Among smaller-scale features that can be imaged with the higher global resolution achievable with today's data are the unusual, conspicuous low-velocity zones beneath cratons in South America and Tanzania, which we suggest reveal hot material—possibly of plume origin—beneath the thick cratonic lithosphere. Detection of these and other regional-scale features by tomographic imaging yields useful new constraints on the dynamics of the upper mantle, which is to be the focus of future work. In this paper, we shall concentrate on the presentation and validation of the tomographic methods and the tomographic model.

## 2 INVERSION SCHEME

Our two-step inversion procedure is an elaborate new implementation of the partitioned waveform inversion scheme introduced by Nolet (1990). In the first step, non-linear waveform inversion extracts information from each seismogram in the form of linear equations with uncorrelated uncertainties (Nolet 1990). This is accomplished with AMI (Lebedev *et al.* 2005). In the second step, we combine the linear equations obtained from all seismograms of the data set and solve the resulting large system for a 3-D earth model.

### 2.1 Automated multimode inversion

In this section, we focus on new additions to AMI but illustrate the waveform inversion with two examples, one for a shorter and another for a longer source-station distance (Figs 1 and 2, respectively). Adopting the JWKB approximation, we compute synthetic seismograms as

$$s(\omega) = \sum_m A_m(\omega) \exp \{ i\omega\Delta [C_m^0(\omega) + \overline{\delta C_m(\omega)}] \}, \quad (1)$$

where the sum is over modes  $m$ , the source–receiver distance is  $\Delta$ , and the initial phase velocities and their path-average perturbations are  $C_m^0(\omega)$  and  $\overline{\delta C_m(\omega)}$ , respectively. The complex amplitudes of the modes  $A_m(\omega)$  depend on the source mechanism and the earth model assumed for the source region, as well as on geometrical spreading and attenuation (Dahlen & Tromp 1998).

The path-average phase-velocity perturbations are expressed as functions of path-averaged *S*- and *P*-velocity perturbations ( $\overline{\delta\beta}$  and  $\overline{\delta\alpha}$ , respectively):

$$\overline{\delta C_m(\omega)} = \int_0^a \frac{\partial C_m^0(\omega)}{\partial\beta(r)} \overline{\delta\beta(r)} dr + \int_0^a \frac{\partial C_m^0(\omega)}{\partial\alpha(r)} \overline{\delta\alpha(r)} dr, \quad (2)$$

where  $a$  is the radius of the Earth.

Phase velocities of fundamental-mode Rayleigh waves  $C_0(\omega)$  are sensitive primarily to *S* velocities, but their sensitivity to *P* velocities is not negligible (Fig. 3), and we parametrize and model both  $\beta$  and  $\alpha$ . Because the derivatives  $\partial C_0(\omega)/\partial\alpha(r)$  peak at shallower depth than do  $\partial C_0(\omega)/\partial\beta(r)$ , potential errors in surface-wave tomography

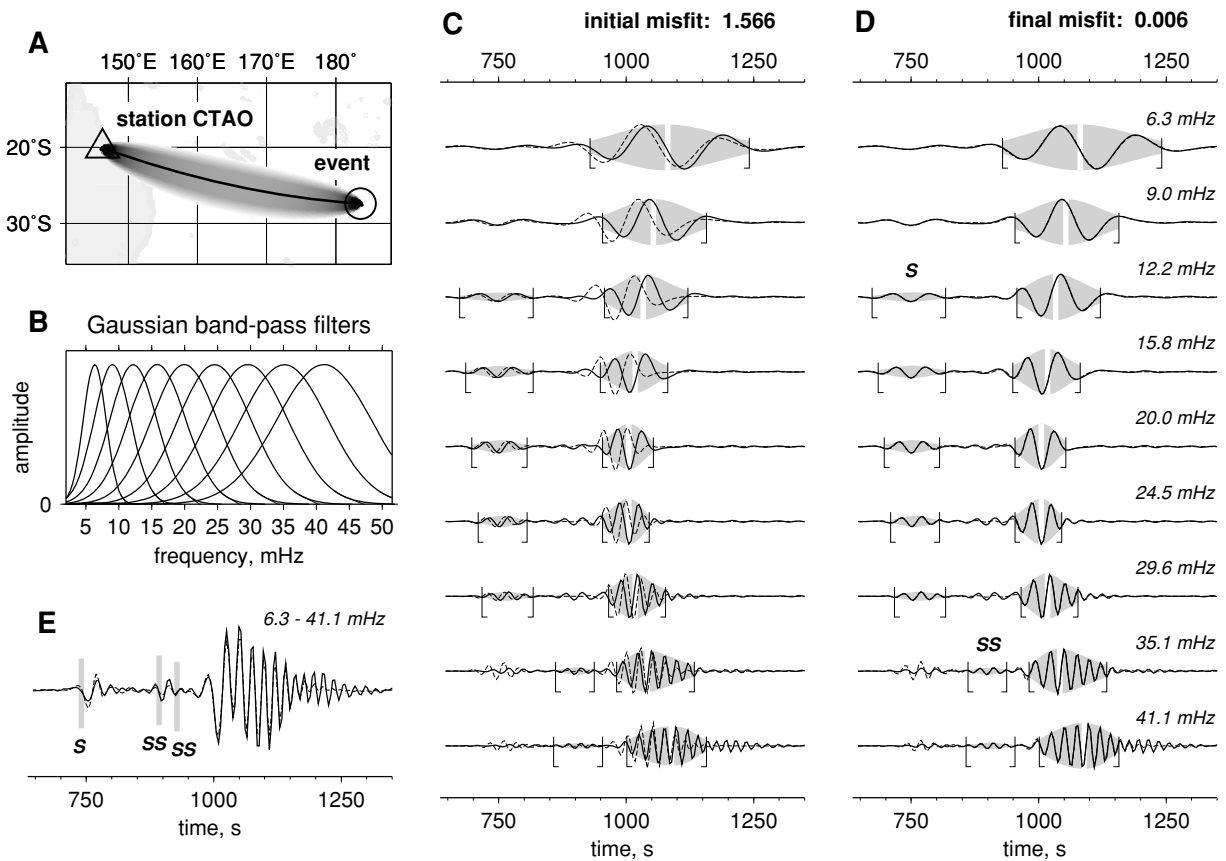


**Figure 1.** Automated multimode inversion. (a) An earthquake on 2002 April 26 (27°S, 176°W, 27 km depth, moment magnitude  $M_w = 5.7$ ) was recorded on the vertical component at the station CTAO (Charters Towers) operated by the Global Seismographic Network (GSN); the source-station distance is 3878 km. The approximate sensitivity area is shaded grey (darker shade for stronger sensitivity); the source-station great circle path (black line) is drawn for reference. (b) The broad-band seismogram is filtered using nine closely spaced Gaussian filters. (c) The resulting waveforms (solid lines) are matched with synthetics (dashed lines) in 16 time-frequency windows simultaneously. The time windows are indicated by half-brackets and by shading of the signal envelope. Fundamental-mode wave trains are identified by white vertical lines at the maxima of the envelope. The initial fit is with synthetics computed for the 3-D background model (eqs 1 and 3). (d) The misfit is minimized through path-averaged perturbations  $\delta\beta(r)$ ,  $\delta\alpha(r)$  (eqs 1–5). The energy of the synthetic is equalized with that of the data in every window. The 16 time-frequency windows selected all have final data-synthetic misfits within them below 5 per cent (Lebedev *et al.* 2005). The path-averaged perturbations inferred in the waveform inversion constrain  $S$ - and  $P$ -velocity tomographic parameters within the sensitivity area shown in (a). (e) Data-synthetic fit within a single, broad time-frequency window (computed after the waveform inversion for illustration purposes only). Arrivals of the  $S$  and triplicated  $SS$  waves predicted by AK135 (Kennett *et al.* 1995) are identified with grey lines and labels in (e);  $S$  and  $SS$  wave trains are also labeled in (d).

due to the neglect of  $P$  velocities would include overestimation of the depth extent of anomalies: if a  $P$ -velocity anomaly at a 50- or 100-km depth is unaccounted for it can be mapped into an artificial  $S$ -velocity anomaly at a 150- or 300-km depth (Fig. 3). We ignore variations in density, however, because their effect on  $\delta C_m(\omega)$  is much smaller than that of those in  $S$  velocity and because they can neither be constrained independently with Rayleigh-wave data, nor coupled to  $S$  velocities in the inversion (seismic-velocity and density variations do not always correlate).

### 2.1.1 3-D reference model

The path-average approximation as formulated in (2) relates average perturbations in seismic velocities  $[\delta\beta(r), \delta\alpha(r)]$  to perturbations in waveforms through  $\delta C_m(\omega)$ . The approximation does not imply that source-station paths have to be represented with geometrical rays; we shall assume instead that  $[\delta\beta(r), \delta\alpha(r)]$  average over finite-width sensitivity areas. It is also not necessary to consider any path-average 1-D models; we shall instead deal with perturbations to a 3-D reference model that are averaged over sensitivity areas.

The reference phase velocities  $C_m^0(\omega)$  and their Fréchet derivatives  $\partial C_m^0(\omega)/[\partial\beta(r), \partial\alpha(r)]$  in (1, 2) should be close to the true averages over the sensitivity areas of the modes. The derivatives, in particular, relate the perturbations in waveforms to  $S$ - and  $P$ -velocity perturbations in the tomographic model, so that their accuracy has a direct effect on the resolution of the imaging: less accurate derivatives result in more inconsistent equations in the tomographic problem; more inconsistency results in noisier images; the inversion then has to be smoothed and damped more heavily, which degrades image resolution.

Recognizing that derivatives  $\partial C_m^0(\omega)/[\partial\beta(r), \partial\alpha(r)]$  computed for the same (e.g. global average) model, regardless of the location of the path, are a very crude approximation, Nolet (1990) proposed to compute them for different 1-D models, each with an estimated average structure of the crust and mantle along the source-station path in question. Choosing such models, however, is not straightforward if the structure changes substantially between the source and the receiver. And there is not even a guarantee that there exists a 1-D model such that the derivatives computed in it for every mode at every frequency will be the same as the averages over derivatives

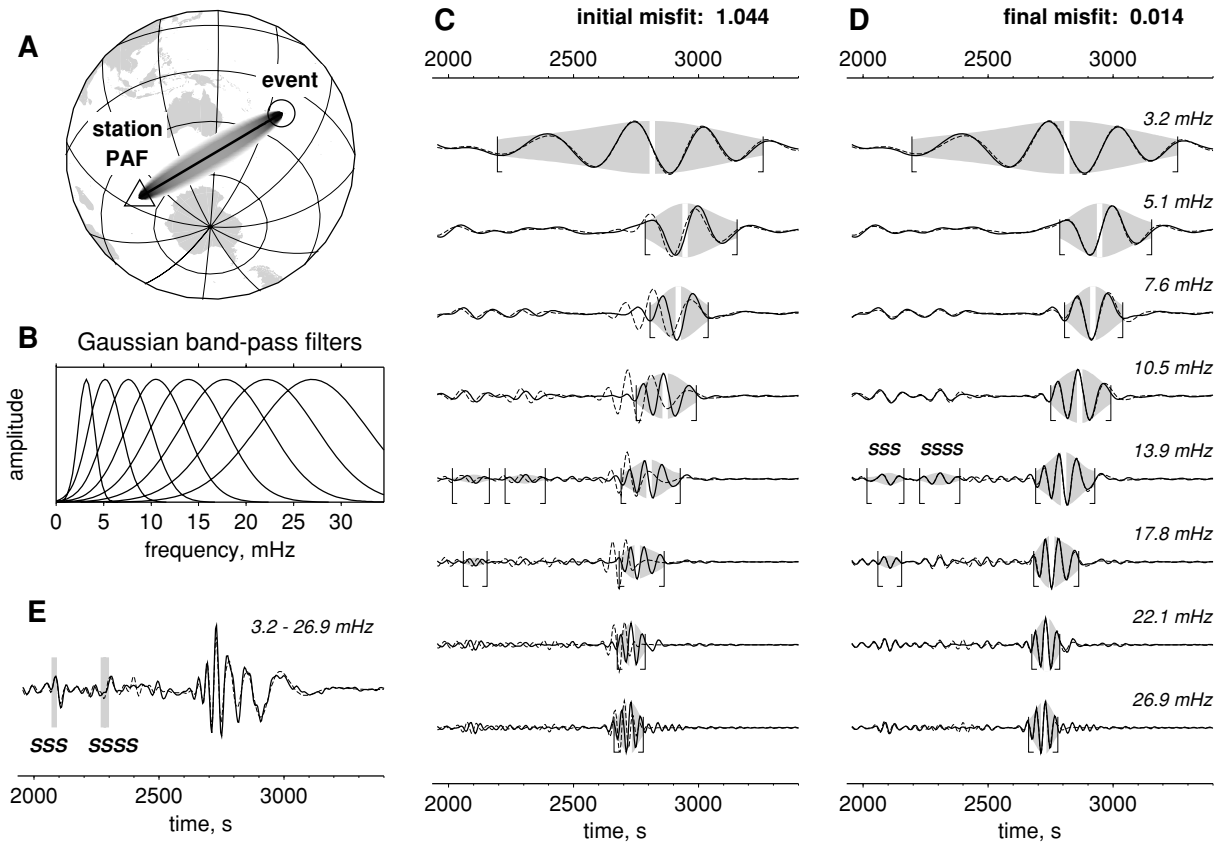


**Figure 2.** Automated multimode inversion. (a) An earthquake on 1996 August 5 ( $15^{\circ}\text{S}$ ,  $173^{\circ}\text{W}$ , 54 km depth,  $M_w = 6.6$ ) was recorded on the vertical component at the station PAF (Port aux Français, Kerguelen Island) operated by Geoscope; the source-station distance is 10 569 km. The plots are as in Fig. 1 except with eight Gaussian filters, 11 time-frequency windows, and arrivals of the SSS and triplicated SSSS waves labelled.

corresponding to the various seismic velocity profiles occurring between the source and the station.

With computational resources available today it is possible to avoid this difficulty. We implemented a direct computation of the averages:

$$C_m^0(\omega) = \int_{\theta} \int_{\phi} \overline{K(\theta, \phi)} C_m(\omega, \theta, \phi) d\phi d\theta, \quad (3)$$

$$\frac{\partial C_m^0(\omega)}{\partial \beta(r)} = \int_{\theta} \int_{\phi} \overline{K(\theta, \phi)} \frac{\partial C_m(\omega, \theta, \phi)}{\partial \beta(r)} d\phi d\theta, \quad (4)$$

$$\frac{\partial C_m^0(\omega)}{\partial \alpha(r)} = \int_{\theta} \int_{\phi} \overline{K(\theta, \phi)} \frac{\partial C_m(\omega, \theta, \phi)}{\partial \alpha(r)} d\phi d\theta, \quad (5)$$

where the integration is over coordinates  $\theta$  and  $\phi$  on the Earth's surface and  $K(\theta, \phi)$  is a sensitivity kernel between the source and the station averaged over the frequency band of the waveform inversion.

We parametrize the Earth's surface with a dense grid of knots (Wang & Dahlen 1995a) and assign a crustal structure to every knot using the global model CRUST2.0 (Bassin *et al.* 2000). We smooth CRUST2.0 near the boundaries of its  $2^{\circ} \times 2^{\circ}$  cells and complement it with topography and bathymetry databases. We then compute  $C_m(\omega)$  and  $\partial C_m(\omega)/[\partial \beta(r), \partial \alpha(r)]$  for the seismic profile beneath every knot. CRUST2.0 defines 360 crust types, each of them defining crustal structure beneath at least one  $2^{\circ} \times 2^{\circ}$  cell on the

globe. Because topography and bathymetry also affect  $C_m(\omega)$  and  $\partial C_m(\omega)/[\partial \beta(r), \partial \alpha(r)]$ , phase velocities and their derivatives are generally different for every point at the Earth's surface, even with the assumption that only 360 crust types can occur. In large portions of the oceans, however, both bathymetry and crustal profiles are relatively uniform. Comparing the derivatives  $\partial C_m(\omega)/[\partial \beta(r), \partial \alpha(r)]$  for various models we identified 664 combinations of crustal types and topography and bathymetry such that one of them provides accurate  $\partial C_m(\omega)/[\partial \beta(r), \partial \alpha(r)]$ —according to CRUST2.0 and topography—at any given knot of our grid covering the Earth's surface.

For the mantle structure below the Moho, we use as a reference for waveform inversions the 1-D model AK135 (Kennett *et al.* 1995) (Fig. 4). We accounted for anelastic dispersion (Liu *et al.* 1976) in the course of waveform inversions assuming the quality-factor ( $Q$ ) profile from AK135. Because lateral variations in attenuation are poorly known at the wavelengths we aim to resolve they were ignored. This would generally give rise to errors in tomographic modelling, and the errors would be larger for larger differences between the reference period assumed and the period of the seismic waves analysed (Liu *et al.* 1976). In order to minimize these errors, we performed waveform inversions for seismic-velocity variations at a reference period of 50 s. This period is close to the middle of a typical frequency band, somewhat shorter than average; we chose it because shorter-period surface waves (20–50 s) are likely to sample the largest variations in  $Q$ , including sharp  $Q$  decreases beneath mid-ocean ridges and backarc basins due to the partial melting in the upper 80–100 km of the mantle there (e.g. Forsyth *et al.* 1998). The

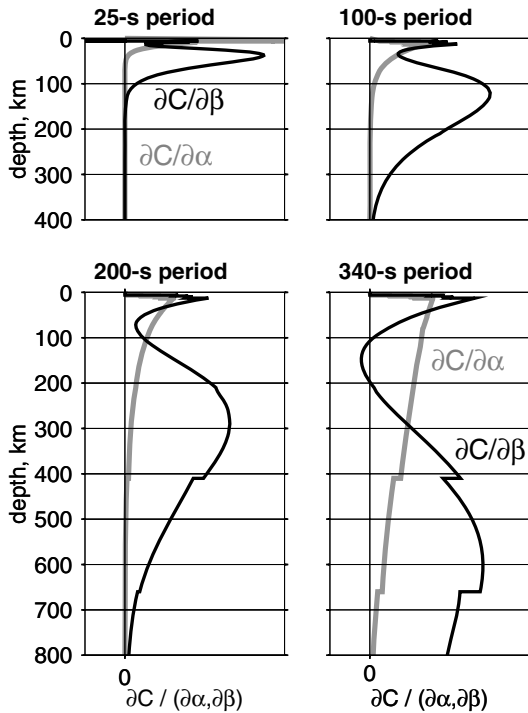


**Figure 3.** Fréchet derivatives of the phase velocity of the fundamental Rayleigh mode with respect to  $P$ - and  $S$ -wave velocities ( $\alpha$  and  $\beta$ ) at different periods included in the data set. Each graph is scaled independently. The derivatives are computed for an oceanic model with a 6-km water layer, a 0.07-km sedimentary layer, and a 6.5-km thick crystalline crust (type-A0 crustal structure of CRUST2.0 but with a thickened water layer).

reference  $S$ - and  $P$ -velocity profiles from AK135 were recomputed from the standard reference period 1 s to the reference period of 50 s using the AK135  $Q$  profile.

For the calculation of  $\partial C_m(\omega)/[\partial\beta(r), \partial\alpha(r)]$  we disregard below-Moho mantle heterogeneity because its effect on the derivatives is usually smaller than that of the crustal structure and the Moho depth. Accounting for mantle heterogeneity would, however, be straightforward with the procedure described here.

Having computed the phase velocities and their derivatives for the 664 type 1-D profiles, we can determine  $C_m(\omega, \theta, \phi)$  and  $\partial C_m(\omega, \theta, \phi)/[\partial\beta(r), \partial\alpha(r)]$  at any point  $(\theta, \phi)$ , and thus compute  $C_m^0(\omega)$  and  $\partial C_m^0(\omega)/[\partial\beta(r), \partial\alpha(r)]$  (eqs 3–5) readily for any source-station path.

### 2.1.2 Sensitivity areas

The kernels  $\overline{K(\theta, \phi)}$  define the sensitivity areas of bandpassed waveform signals. We postulate the sensitivity areas  $\overline{K(\theta, \phi)}$  to be bounded by the perimeter of the ‘ $\pi/2$ ’ Fresnel zone (enclosing all points such that the phase shift between the wave propagating from the source to the point and then to the receiver and the wave propagating from the source directly to the receiver would not exceed  $\pi/2$ ) (Figs 6 and 7). The  $\pi/2$  Fresnel-zone boundary is given by

$$\delta = \sqrt{\frac{\lambda/2}{|\cot\Delta_1 + \cot\Delta_2|}}, \quad (6)$$

where  $\Delta_1$  and  $\Delta_2$  are the distances from a point on the source-station great circle path to the source and to the receiver,  $\delta$  is the path-normal distance from this point to the Fresnel-zone boundaries, and  $\lambda$  is the wavelength (Wang & Dahlen 1995b). All distances are measured

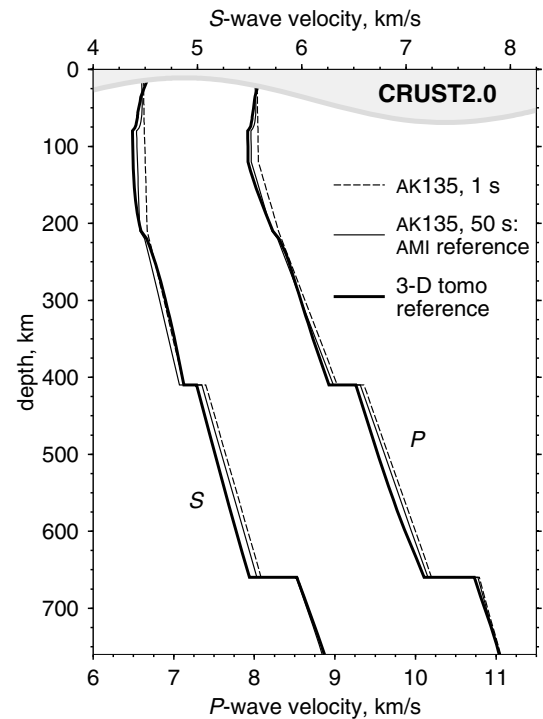


**Figure 4.** Reference models. The reference model used for waveform inversions is composed of the 3-D crust of CRUST2.0 (Reference Earth Model web site, <http://mahi.ucsd.edu/Gabi/rem.html>) and—below the Moho—the 1-D AK135 (Kennett *et al.* 1995) recomputed at a reference period of 50 s. In the inversion for the 3-D tomographic model, we use as a mantle reference profile the global average that results from our tomography (thick line).

in radians. Because we use one average  $\overline{K(\theta, \phi)}$  per seismogram (eqs 2–5), we compute  $\lambda$  as the average fundamental-mode wavelength within the frequency band in which the fundamental mode is inverted.

In cross-section perpendicular to the path the kernels  $\overline{K(\theta, \phi)}$  are trapezoidal, with a constant grid-knot weight within their middle portions and a gradual decrease to zero within their peripheral portions (Fig. 7). This shape is similar to that of the empirical stationary phase function of Yoshizawa & Kennett (2002) (their fig. 9, real part) as well as to that of phase-velocity-measurement sensitivity kernels (Zhou *et al.* 2005, their fig. 17), truncated at the first zero crossing. The integral over a path-normal section through the kernel is constant, so that the knots close to the source or receiver have larger weights than those close to the middle of the path (Fig. 6). Behind the source and the receiver (where either of the distances to the source or to the receiver exceeds the source–receiver distance) the kernel is tapered to zero. Because the kernels represent the sensitivity of the waveform data more accurately than geometrical rays, we use them in both the waveform inversions (eqs 1–5) and the 3-D tomographic inversion (Section 2.2), even though the resolution of upper-mantle imaging may at present be limited more by the unevenness of global data coverage (Trampert & Spetzler 2006) and errors in source parameters than by approximations in sensitivity mapping.

### 2.1.3 Path-average-approximation validity

Eqns (4) and (5) enable an accurate implementation of the path-average (more precisely, sensitivity-area-integral) approximation. The validity of the approximation, however, is still not guaranteed.

The criterion of its validity may in general terms be thought of as

$$\frac{\partial C_m(\omega, \theta, \phi)}{\partial \beta(r)} \approx \frac{\partial C_m^0(\omega)}{\partial \beta(r)}, \quad \forall (\theta, \phi) : \overline{K(\theta, \phi)} > 0 \quad (7)$$

(the derivatives at every point within the sensitivity area are approximately equal to the derivatives averaged over the area); it may not be satisfied for paths sampling strong lateral heterogeneity, for example, those across continent–ocean boundaries.

To apply the criterion (7) in data processing we formulated it in terms of the waveform fit  $F$ :

$$\delta F_i = \int |\overline{s^{\partial C/\partial \beta}}(t) - s^{\partial C(\theta, \phi)/\partial \beta}(t)|^2 / |\overline{s^{\partial C/\partial \beta}}(t)|^2 dt; \quad (8)$$

$$\delta F_i < \epsilon, \quad \forall (\theta, \phi) : \overline{K(\theta, \phi)} > 0. \quad (9)$$

Within the  $i$ th time-frequency window, the misfit  $\delta F_i$  between the synthetics that are computed using path-averaged derivatives  $\partial C/\partial \beta$  and using derivatives  $\partial C(\theta, \phi)/\partial \beta$  for a 1-D  $[\beta(r), \alpha(r)]$  profile beneath any point  $(\theta, \phi)$  within the sensitivity area of the waveform must not exceed a threshold  $\epsilon$ . The synthetics are computed using the path-averaged perturbations  $[\overline{\delta \beta(r)}, \overline{\delta \alpha(r)}]$  that have already minimized the data–synthetic misfit, so that  $\delta F_i$  is the extra misfit due to the approximation. Provided that misfits are small—and AMI accepts relative data–synthetic misfits below 5 per cent only—they are directly related to the uncertainties of the linear constraints on Earth structure yielded by the waveform inversion (Nolet 1990; Lebedev *et al.* 2005).

We have reprocessed our entire data set repeatedly while enforcing the validity of the path-average approximation using different values of  $\epsilon$ . Tight thresholds resulted in rejection of most of fundamental-mode time-frequency windows at higher frequencies (30–60 mHz) and a subsequent loss of vertical resolution in the upper  $\sim 50$  km of the model. More important, however, if not somewhat surprising, was that deeper structure was affected only weakly. In the following, we present a model computed using all data but with a 0.044 Hz (period 23 s) high-frequency limit for the centre frequency of a Gaussian filter (Figs 1 and 2).

## 2.2 Linear inversion

The result of the waveform inversion is a set of  $M$  equations with uncorrelated uncertainties  $\Delta \eta_i$ :

$$\int_{\oplus} [G_i^\beta(\mathbf{r}) \delta \beta(\mathbf{r}) + G_i^\alpha(\mathbf{r}) \delta \alpha(\mathbf{r})] d^3 \mathbf{r} = \eta_i \pm \Delta \eta_i, \quad (10)$$

where  $i = 1, \dots, M$ . The vertical structure of the kernels  $G_i^{(\beta, \alpha)}(\mathbf{r})$  depends on how this particular waveform is related to (and, thus, constrains) the path-averaged perturbations  $[\overline{\delta \beta(r)}, \overline{\delta \alpha(r)}]$  (Nolet 1990; Lebedev *et al.* 2005); their horizontal structure is the same as that of the  $\overline{K(\theta, \phi)}$  used in the waveform inversion. The transformed data vector (Nolet 1990) is denoted by  $\eta_i$ . Combining the equations obtained from all seismograms, we build a large system of linear equations and solve it using LSQR with lateral and radial smoothing and norm damping.

The sensitivity areas  $\overline{K(\theta, \phi)}$  are evaluated at knots of a dense integration grid. This global triangular grid of knots with an approximately equal interknot spacing of, on average, 28 km is computed following Wang & Dahlen (1995a) (Figs 5 and 6). For every knot, we identify the hexagon around it that contains all points that are closer to this than any other knot. A few knots of such a global triangular grid have five rather than six closest-neighbour knots (Fig. 5); for

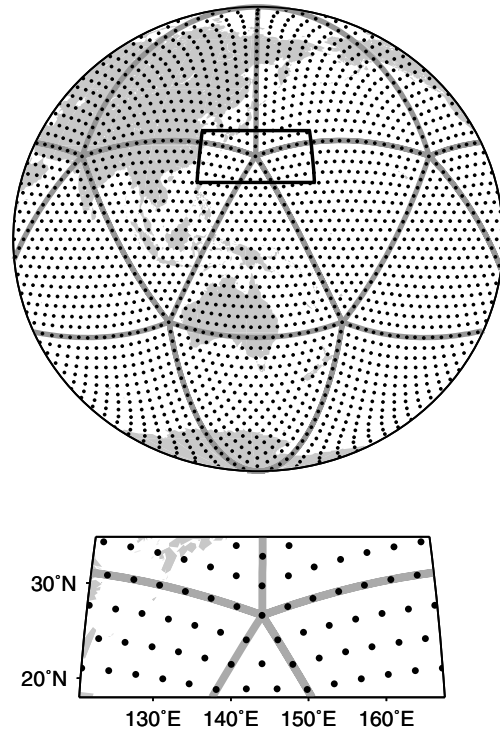


**Figure 5.** The model grid. This global triangular grid (Wang & Dahlen 1995a) with an approximately constant interknot spacing of  $3.5^\circ$  was used to parametrize the tomographic inversion.

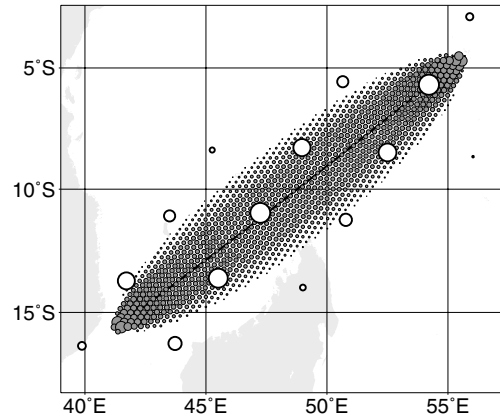


**Figure 6.** A sensitivity area (kernel)  $\overline{K(\theta, \phi)}$  as sampled by the integration and model grids. The source-station distance is 1950 km; the frequency range of the fundamental-mode time-frequency windows is 11–33 mHz. The grey circles show the knots of the dense integration grid used to sample the structure of the sensitivity area. Circle sizes scale with the weights of the knots in the integral over the area. The white circles show knots of the model grid. Circle sizes scale with the weights of the model parameters in eq. (10).

these knots the neighbourhood area around them is a pentagon. We compute the areas of the hexagons (pentagons) around the knots; the areas vary by up to 20 per cent.  $\overline{K(\theta, \phi)}$  is calculated at each knot and multiplied by the area of the hexagon (pentagon) around to yield the weight of the knot in the integral over the sensitivity area.

We also define a model grid (Figs 5 and 6), with interknot spacing of  $3.5^\circ$ .  $S$ - and  $P$ -velocity perturbations at the locations of these knots are the unknowns in the inversion. The same shell of knots is

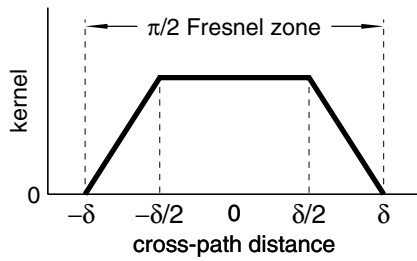


**Figure 7.** A cross-section through the sensitivity kernel perpendicular to the source-station great circle path.  $\delta$  is the half-width of the ' $\pi/2$ ' Fresnel zone which contains all points such that the phase shift between the wave propagating from the source to the point and then to the receiver and the wave propagating from the source directly to the receiver would not exceed  $\pi/2$ .

used at all depths, with 18 parameters vertically for  $S$  velocity (knots at 7, 20, 36, 56, 80, 110, 150, 200, 260, 330, 410–, 410+, 485, 585, 660–, 660+, 809 and 1007 km depths) and 10 parameters for  $P$  velocity (knots at 7, 20, 36, 60, 90, 150, 240, 350, 485 and 585 km depths). The kernels  $G_i^{(\beta, \alpha)}(\mathbf{r})$  are evaluated at the model grid knots by integrating over the neighbouring integration-grid knots.

(In order to verify that the 28 km knot spacing of the integration grid is sufficiently small for an accurate integration over the approximate sensitivity areas we have recomputed the kernel shown in Fig. 6 using 30 km integration-grid knot spacing. The average difference between the values of the kernel at the model-grid knots that were computed with 28 and 30 km integration-grid spacing was only 0.005 (the maximum, 0.02) of the largest value of the kernel at a model-grid knot for the path—negligible for this approximate kernel.) With a mapping between the two grids established in the beginning of the procedure, the large linear inverse problem can be set up readily.

Occurrences of bundles of similar rays, some with hundreds of nearly identical source-station paths, can bias the tomographic image. Due to the nature of the waveform inversion— $G_i^{(\beta, \alpha)}(\mathbf{r})$  are generally different for every seismogram, depending on the frequency band of the inversion and the higher-mode content of the waveforms—information from such bundles of similar paths cannot be summarized as is done with 'summary rays' in traveltime tomography. Instead, we identify similar paths and down-weight each of them according to the number of paths that are similar to it and to how close the sources and receivers of similar paths are to each other (Fig. 8).

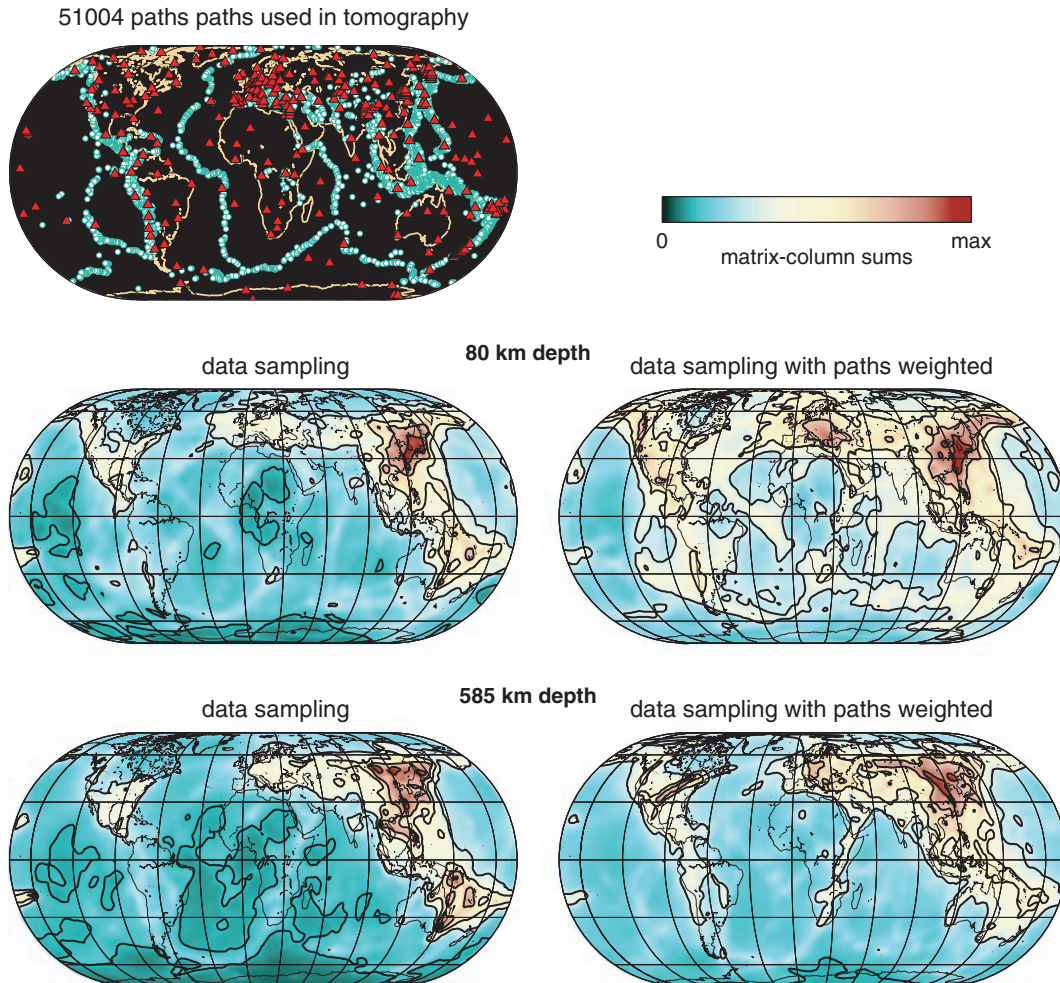


**Figure 8.** Top: the dense coverage of the globe with the  $\sim 51\,000$  source-station paths. Earthquakes used are plotted as circles, stations as triangles. Below: relative data sampling without and with path weighting at two depths. The measure of data sampling is the sums of the columns of the matrix that relates the data to the model, with each column corresponding to one parameter. We plot sums of shear-velocity-parameter columns. The colour-scale limits are different for every frame, scaled to the maximum of each distribution.

The smoothness constraints on the inversion penalize the difference between the anomaly at a knot and the average over anomalies at this and the six (in a few cases, five) (Fig. 5) closest-neighbour knots. The strength of the lateral smoothing varies from one depth to another, so as not to oversmooth excessively in the lower half of the upper mantle where data sampling is much weaker than in its upper half. The data sampling is quantified using averages of the sums of the matrix columns which correspond to the model parameters at the depth.

We found that  $P$ -velocity perturbations could not be resolved independently with Rayleigh-wave data and chose to damp the difference between  $P$ - and scaled  $S$ -velocity perturbations; we penalized the difference  $|\delta V_P(\text{m s}^{-1}) - \delta V_S(\text{m s}^{-1})|$ . This gives the inversion more flexibility than imposing a rigid  $\delta \ln V_P / \delta \ln V_S$  ratio. The  $P$ - and  $S$ -velocity images are still similar, and we shall present only the latter.

We also allowed for azimuthal anisotropy in  $S$  velocities and found that patterns of its distribution can be retrieved only with much lower resolution than those in isotropic heterogeneity, as has been reported previously (e.g. Simons *et al.* 2002; Debayle *et al.* 2005). In this study, our motivation to account for anisotropy was to reduce errors due to trade-offs between isotropic and anisotropic heterogeneity, and we present only the isotropic part of the model; anisotropic heterogeneity itself shall be the focus of future work.

The reference mantle profile used in the inversion for the 3-D tomographic model is derived in our initial inversions: it is close to the global average as constrained by our data (Fig. 4, thick line).

### 3 DATA

We can expect AMI to improve the resolution in the upper mantle because it produces unique sets of constraints on Earth structure. In this study, we extract structural information from fundamental mode wave trains containing substantial energy at periods from 20 to 400 s (a very broad frequency band) and recorded at distances from <1000 to 15 000 km (both short regional and long teleseismic paths), as well as from  $S$  and multiple  $S$  waves ( $SS$ ,  $SSS$ ,  $SSSS$ ,  $SSSSS$ ) that bottom in the upper mantle or uppermost lower mantle. The  $S$  and multiple  $S$  waves are often triplicated and are particularly sensitive to the transition-zone structure. The waveforms of both the  $S$  waves and the very-long-period (>200 s) fundamental-mode Rayleigh waves constrain seismic-velocity structure in the lower half of the upper mantle, down to the 660 km depth.

The vertical-component, long-period and broad-band seismograms were retrieved from IRIS DMS. We used data recorded from 1994 to 2002 at stations of the GSN, Geoscope, Geofon, China Digital Seismograph Network (CDSN), Canadian National Seismic Network (CNSN), Kaznet, MEDNET and POSEIDON, as well as a number of PASSCAL experiments—368 stations in total (Fig. 8).

We discarded the ‘near-nodal’ signal as well as clipped and defective recordings (Lebedev *et al.* 2005) and obtained waveform fits for ~80 000 seismograms. Centroid Moment Tensor (CMT) solutions for the source mechanisms of the events were taken from the Harvard catalogues (e.g. Dziewonski *et al.* 1994). Because of the probable trade-offs between different source parameters, event locations and origin times were also taken from the Harvard catalogues.

We expect the locations and origin times of the events to be the largest source of errors in the tomographic inversion, but these errors are difficult to estimate. In an attempt to remove data with a greater probability of large location-related errors, we compared locations and origin times from the Harvard and the short-period EHB (Engdahl *et al.* 1998) catalogues. We computed the discrepancies

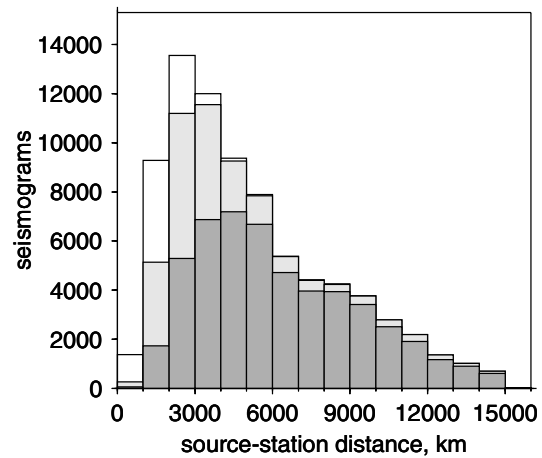


**Figure 9.** Distribution of source-station paths used in tomography with distance. White: the initial set of waveform fits, ~80 000 source-station pairs. Light grey: ~71 000 source-station pairs with smaller estimated effects of suspected location errors. Dark grey: the final data set of ~51 000 source-station pairs, obtained after the ‘outlier’ seismograms (those fit the worst by the 3-D tomographic model) are discarded.

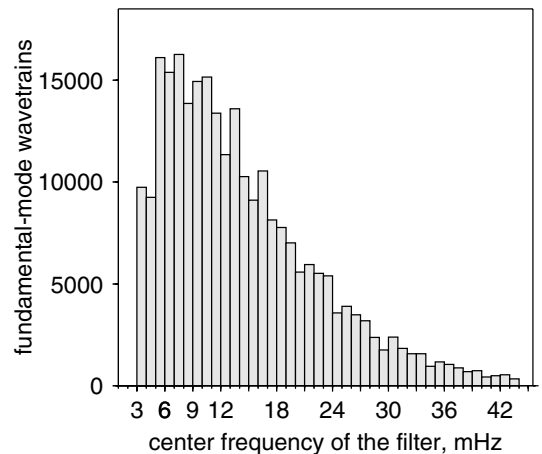


**Figure 10.** Distribution of the fundamental-mode wave trains of the data set with frequency (the centre frequency of the Gaussian filters used to define the time-frequency windows with the wave trains).

in hypothetical phase-velocity measurements at every station that recorded the event due to the difference of epicentre locations from the different catalogues, due to the difference between the origin times, and due to the combined effect of differences in both the locations and origin times. Rejecting paths with largest discrepancies according to each of the three criteria, we discarded about 10 per cent of the data (mostly shorter paths) and obtained a data set of ~71 000 seismograms (Fig. 9).

In the final stage of data selection, we computed a model constrained with the ~71 000 seismograms and examined how well it fits the data. Poor fit for a path can be indicative of a mislocation, of a timing error at the station, or of errors in our modelling of the waveform-data sensitivity. Discarding the worst-fitting, ‘outlier’ paths, we computed a new model, then discarded outliers again and finished with the 51 004 paths of our final data set (Figs 8 and 9).

Long paths (Fig. 9) ensure dense global coverage, whereas shorter paths offer higher resolution in regions of denser sampling with

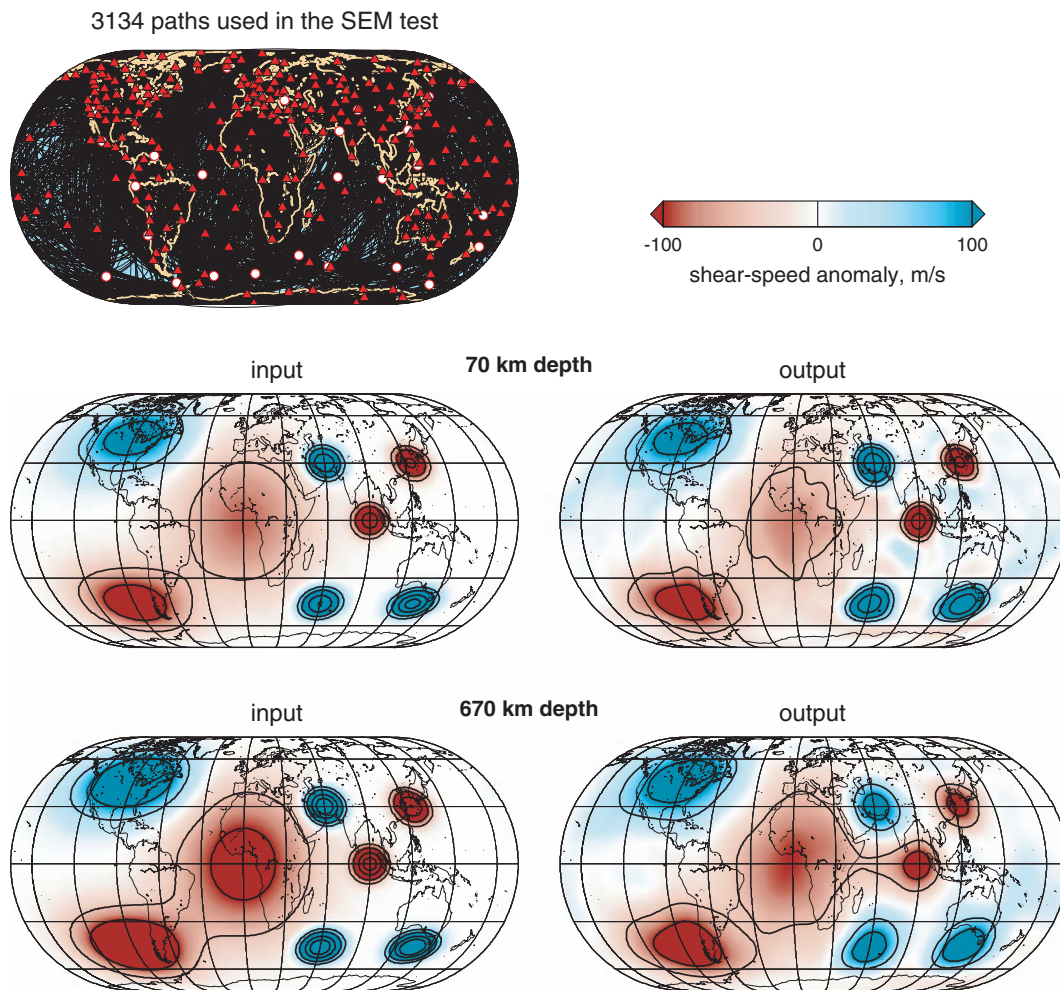


**Figure 11.** The SEM-benchmark resolution test. Inverting the synthetic seismograms computed by Qin *et al.* (2006) with the spectral-element method and their benchmark, laterally heterogeneous global model, we reconstruct the input model. On the map on top, sources and stations used in the test are plotted as circles and triangles, respectively; source-station great circle paths are shown with black lines. The cross-sections below show the synthetic and retrieved anomalies at the 70-km and 670-km depths. Contours are drawn at  $\pm 50$ ,  $\pm 100$ ,  $\pm 200$  and  $\pm 300$   $\text{m s}^{-1}$ .

both sources and stations (e.g. East Asia). The very-long-period Rayleigh waves (centre frequency of the filter below 5 mHz) are included for  $\sim 19\,000$  paths (Fig. 10) and sample the lower half of the upper mantle (Fig. 3). For our lowest-frequency filters centred at 3.17 mHz (period 315 s), the amplitude of the filter curve is still above 0.5 of the maximum of the curve at the frequency of 2.2 mHz (period 450 s) (Fig. 2). We estimate that longest-period wave trains of our data set contain substantial energy—and contribute structural constraints—at periods at least up to 400 s.

#### 4 SEM RESOLUTION TEST

For benchmark purposes, Qin *et al.* (2006) constructed a laterally heterogeneous global model and computed synthetic seismograms in it using the spectral-element method (Capdeville *et al.* 2003). We have inverted the synthetic waveforms using the same criteria as when processing real data (Sections 2 and 3) and computed a 3-D model with the same definition of regularization as in inversion of the data; the smoothing and damping coefficients were smaller than in the data inversion because the sampling of the upper mantle with the  $\sim 3000$  synthetics was much sparser than that with the  $\sim 51\,000$  actual seismograms.

The input model is reconstructed accurately (Fig. 11). At lithospheric depths, especially in Asia and North America where the synthetic path coverage is the densest, we retrieve both the shape and the amplitude of the anomalies. At the bottom of the transition zone the smaller anomalies are underestimated in amplitude by up to a factor of 2 but mapped correctly.

This test is more illuminating than conventional resolution tests in that it verifies the validity of assumptions and approximations as used by the tomographic technique as well as the correctness of its implementation. The recovery of the model suggests that AMI accurately selects the portions of the signal for which the assumed JWKB approximation is valid—that is, the effects of seismic-wave scattering are negligible—and that our approximate sensitivity areas  $\bar{K}(\theta, \phi)$  (Figs 1 and 2, eqs 3–5) represent the actual sensitivity of the waveforms sufficiently well. In particular, our neglect of the 3-D structure of the sensitivity volumes of body waves—which could lead to biases in the deeper part of the upper mantle (Marquering *et al.* 1996)—has not prevented the retrieval of the synthetic anomalies in the transition zone. We expect that such biases in the inversion of both the synthetic and real data have been reduced due to the density of data coverage, due to our use of numerous multiple  $S$  waveforms—whose sensitivity volumes (Marquering *et al.* 1998)

are approximated reasonably well by path-average modelling,— and due to our use of very-long-period fundamental-mode surface waves. One possible remaining effect is the underestimation of the amplitude of the smaller anomalies in the transition zone. The magnitude of amplitude biases can be estimated using resolution tests (Lebedev *et al.* 2003), with ‘SEM tests’ (Fig. 11) being potentially the most effective. In order to avoid such biases, sensitivity volumes of the waveform data may have to be modelled explicitly (Meier *et al.* 1997).

## 5 MODEL

In map views of  $S_v$ -velocity variations in the upper 100 km of the mantle (Fig. 12a), mantle regions beneath mid-ocean ridges and backarc basins are marked by low-velocity anomalies. Stable continents are associated with high velocities.

Sharp velocity contrasts are observed across many known tectonic boundaries. Across subduction zones, for instance, we observe sharp transitions from high-velocity oceanic lithosphere to low-velocity volcanic arc regions.

At the 150-km depth the low- $S_v$ -velocity anomalies beneath mid-ocean ridges are no longer visible, except for a number of particular locations (mostly beneath ocean islands). The dominant features at this depth are the high-velocity anomalies beneath ancient cratons as well as beneath zones of subduction and continental convergence.

At 260 km (Fig. 13a) the seismic expression of cratonic lithosphere is already largely absent. Beneath most cratons, no anomaly or very weak fast anomaly (probably indistinguishable from zero given the likely trade-offs with the structure above) is observed. The thickness of the high-velocity seismic lithosphere of cratons is thus not required to exceed  $\sim 200$  km. A similar inference has previously been made by Debayle *et al.* (2005).

Pronounced low-velocity zones (LVZs) are absent beneath most cratons. Notable exceptions (Fig. 13a) are beneath the cratons of central and northern South America and beneath the Tanzanian Craton (around 4°S, 34°E). The anomalous LVZs beneath both locations have been constrained independently by interstation measurements of surface-wave dispersion (Weeraratne *et al.* 2003; Boonen & Lebedev 2005). The subcratonic LVZ beneath Tanzania has been suggested (Weeraratne *et al.* 2003) to represent the seismic expression of the plume feeding the East-African Rift System volcanism. For the LVZ beneath South American cratons, we propose here that the observed anomaly is related to hot (plume?) material ‘ponded’ under cratonic lithosphere as suggested by Sleep (2003) in order to explain hotspot-like volcanism near South American eastern shores.

In the transition zone (Fig. 13) the most conspicuous high-velocity anomalies are beneath areas of current and recent subduction, including those in the Western Pacific, Eastern Asia, Northern Mediterranean, Western North America and Western South America. Further interpretation of the tomographic model in terms of regional and global mantle dynamics will be pursued in future publications.

## 6 DISCUSSION

To verify the accuracy of our tomographic imaging, we have used two kinds of ‘ground-truth’ testing. In one, we have observed that velocity contrasts that are known to be present in the mantle (e.g. across subduction zones) are present in our model as well. In the other, we have inverted the synthetic seismograms computed

(almost) exactly through a heterogeneous mantle model with the SEM (Qin *et al.* 2006) and have been able to retrieve the input model.

The tests confirm that the tomographic method presented in this paper produces accurate images of the upper mantle. In particular, our use of the information from very-long-period, fundamental-mode surface waves and from  $S$  and multiple- $S$  waves (interfering higher modes) is effective in extending the depth range of the imaging down to the bottom of the transition zone (660 km depth).

We have investigated the limits of validity of the path-average approximation and formulated quantitative criteria for it. Re-inverting our global data set with strict validity criteria, we didn’t observe an improvement in resolution at any depth (at shallow depth, the resolution deteriorated because of the exclusion of most high-frequency fundamental-mode data). This result suggests that the effect of the remaining errors due to the assumption of constant phase-velocity derivatives across the sensitivity area is relatively minor compared to that of other errors. The locations, origin times, and source mechanisms of the events probably represent the largest source of systematic errors that affect tomographic images. The full automation and numerical efficiency of our method may help to address this problem directly in the future, inverting for source parameters and 3-D structure in the same procedure, simultaneously or iteratively.

The new implementation of the waveform inversions with a 3-D reference model improves the accuracy of synthetic seismograms and of the structural constraints extracted from waveforms. We have verified this by re-processing a subset of 25 000 seismograms both with a 3-D reference model and with 1-D reference models. The 1-D models were averaged from CRUST2.0 type profiles, the averaging being over thicknesses of and velocities within crustal layers. Phase velocities of the modes and their derivatives  $\partial C_m(\omega)/[\partial \beta(r), \partial \alpha(r)]$  were computed for such averaged 1-D models. AMI was able to obtain an acceptable fit (relative data-synthetic misfit  $< 5$  per cent) in 14 per cent more fundamental-mode time-frequency windows with the 3-D model than with 1-D models. The improvement was not because of the small differences in the initial average synthetic phase velocities between sources and stations—waveform inversions would easily compensate for those with structural perturbations—but, apparently, because relative values of phase velocities and of their derivatives were more consistent with the seismic properties of the Earth when computed in the 3-D reference model rather than in 1-D ones.

## 7 CONCLUSIONS

We have implemented the Automated Multimode Inversion (AMI) of surface- and  $S$ -wave forms (Lebedev *et al.* 2005) with a 3-D reference model, processed a large global data set, and computed an  $S_v$ -velocity model of the upper mantle (crust–660 km depth) constrained by  $\sim 51$  000 waveforms. The tomographic methods rely on the JWKB and path-average approximations (the averaging being over approximate sensitivity areas); we suggest that this basis is adequate for upper-mantle imaging with a resolution of a few hundred kilometres.

Application of AMI to the synthetic data set computed with SEM (Qin *et al.* 2006) showed accurate retrieval of the synthetic model and confirmed that the technique can correctly relate waveform phase information to Earth structure from the uppermost mantle down to the bottom of the transition zone.

Our new tomographic scheme enables fast, accurate integration over paths or sensitivity areas using a pair of triangular grids of knots with approximately equal interknot spacing within each. As

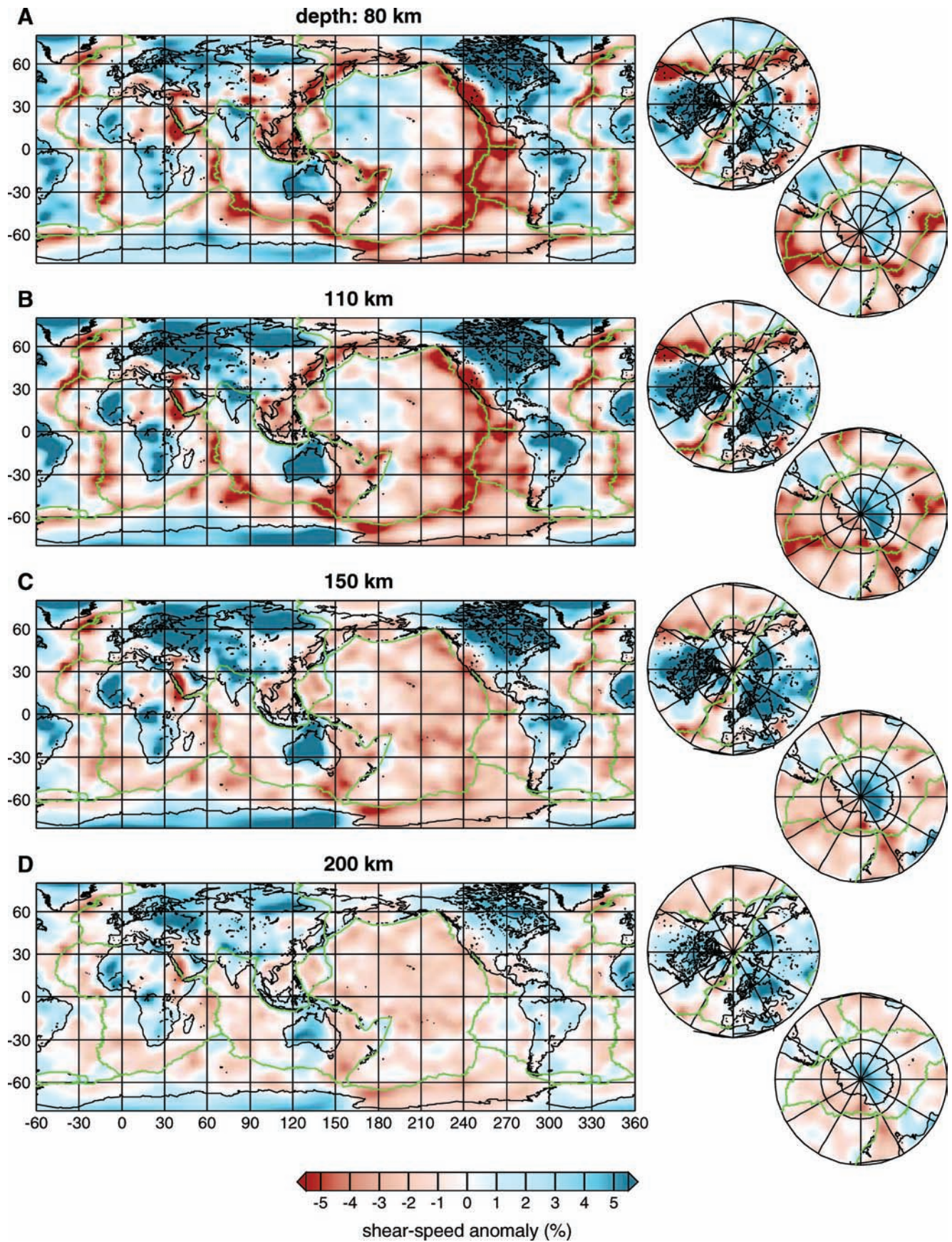


**Figure 12.** Cross-sections through the tomographic model at four depths in the shallower upper mantle. Approximate plate boundaries are shown with green lines. The reference  $S_V$ -wave velocity values are  $4.38 \text{ km s}^{-1}$  (a, b),  $4.39 \text{ km s}^{-1}$  (c),  $4.45 \text{ km s}^{-1}$  (d)—all at a reference period of 50 s.

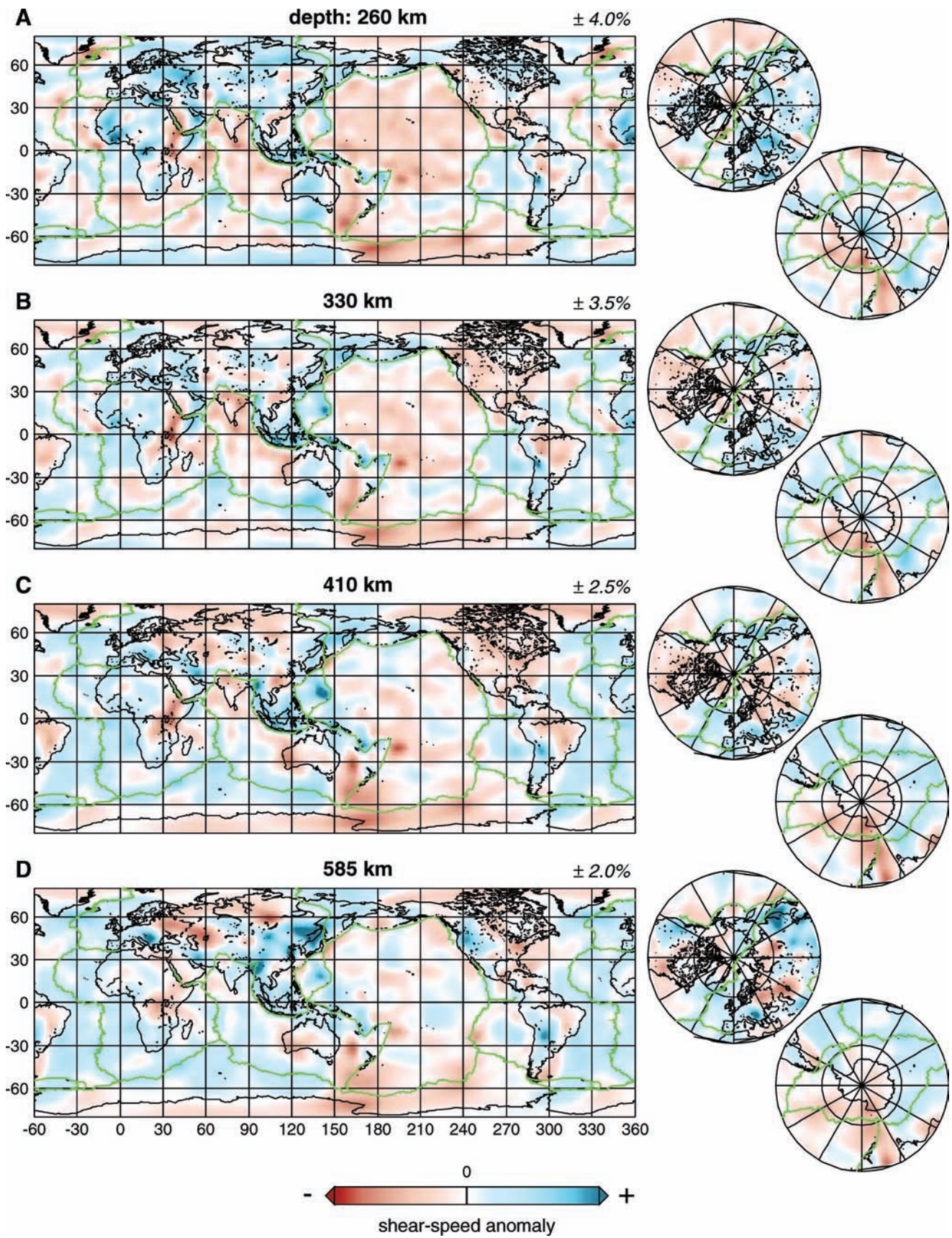


**Figure 13.** Cross-sections through the tomographic model at four depths in the deep upper mantle. The limits of the saturated colour scales are indicated next to each frame. Approximate plate boundaries are shown with green lines. The reference  $S_V$ -wave velocity values are  $4.62 \text{ km s}^{-1}$  (a),  $4.75 \text{ km s}^{-1}$  (b),  $4.99 \text{ km s}^{-1}$  (c),  $5.34 \text{ km s}^{-1}$  (d)—all at a reference period of 50 s.

well as for 3-D tomography as in this study, it can also be applied to other tomographic problems. With AMI itself already being used for measurements of broad-band dispersion of surface-wave modes (e.g. Lebedev *et al.* 2006), the new tomographic scheme can be used for isotropic and anisotropic phase-velocity mapping at global or regional scales (e.g. Zhang *et al.* 2007).

We observe that low- $S_v$ -velocity anomalies beneath mid-ocean ridges extend down to  $\sim 100$  km depth; this is consistent with the limit of the primary melt-production depth range inferred from MELT experiment observations and petrological arguments (Forsyth *et al.* 1998).

Pronounced seismic lithosphere beneath cratons extends down to  $\sim 200$  km. Low-velocity zones are weak or absent beneath most cratons. Exceptions include pronounced LVZs beneath cratons in South America and Tanzania. We suggest that the broad LVZ beneath central and northern South America is a seismic image of hot material, possibly of plume origin, trapped—or ‘ponded’ (Sleep 2003)—beneath the thick cratonic lithosphere.

## ACKNOWLEDGMENTS

We thank Yilong Qin, Yann Capdeville, Valerie Maupin and Jean-Paul Montagner who shared with us the SEM synthetic seismograms computed in their ‘benchmark of the benchmark’ model and Jeannot Trampert who first suggested the ‘SEM test’ of our tomographic technique and whose isotropic and anisotropic inversion experiments with our phase-velocity measurements (a byproduct of waveform inversions) have motivated us to account for azimuthal anisotropy in our tomographic inversion. Comments from anonymous reviewers have helped us to improve the manuscript. Figures were generated with Generic Mapping Tools (Wessel & Smith 1995). Waveform data were obtained from facilities of the Incorporated Research Institutions for Seismology (IRIS) Data Management System (DMS), funded through the National Science Foundation (NSF) GEO Directorate, Instrumentation and Facilities Program, under Cooperative Agreement EAR-0004370. GSN is operated jointly by the IRIS, the United States Geological Survey (USGS), and the NSF. This work was supported by the David and Lucile Packard Foundation Fellowship and the VICI Innovative Research Award, awarded to R. D. van der Hilst.

## REFERENCES

- Bassin, C., Laske, G. & Masters, G., 2000. The current limits of resolution for surface wave tomography in North America, *EOS, Trans. Am. geophys. Un.*, **81**, F897.
- Bijwaard, H., Spakman, W. & Engdahl, E.R., 1998. Closing the gap between regional and global travel time tomography, *J. geophys. Res.*, **103**, 30 055–30 078.
- Boschi, L. & Ekström, G., 2002. New images of the Earth’s upper mantle from measurements of surface wave phase velocity anomalies, *J. geophys. Res.*, **107**, doi:10.1029/2000JB000059.
- Boonen, J. & Lebedev, S., 2005. Anisotropic seismic structure beneath cratons from interstation surface-wave dispersion measurements on GSN and Geofon data, *EOS, Trans. Am. geophys. Un.*, **86**(52), Fall Meet. Suppl., T13A-0439.
- Capdeville, Y., Chaljub, E., Vilotte, J.-P. & Montagner, J.-P., 2003. Coupling the spectral element method with a modal solution for elastic wave propagation in global earth models, *Geophys. J. Int.*, **152**, 34–67.
- Cara, M. & Lévêque, J.-J., 1987. Waveform inversion using secondary observables, *Geophys. Res. Lett.*, **14**, 1046–1049.
- Dahlen, F.A. & Tromp, J., 1998. *Theoretical Global Seismology*, Princeton University Press, Princeton.
- Debayle, E., Kennett, B.L.N. & Priestley, K., 2005. Global azimuthal seismic anisotropy and the unique plate-motion deformation of Australia, *Nature*, **433**, 509–512.
- Dziewonski, A.M., Ekström, G. & Salganik, M.P., 1994. Centroid-moment tensor solutions for January–March 1994, *Phys. Earth planet. Inter.*, **86**, 253–261.
- Ekström, G., Tromp, J. & Larson, E.W.F., 1997. Measurements and global models of surface waves propagation, *J. geophys. Res.*, **102**, 8137–8157.
- Engdahl, E.R., van der Hilst, R.D. & Buland, R., 1998. Global teleseismic earthquake relocation with improved travel times and procedures for depth determination, *Bull. seism. Soc. Am.*, **88**, 722–743.
- Forsyth, D.W., Scheirer, D.S., Webb, S.C. & MELT Seismic Team, 1998. Imaging the deep seismic structure beneath a mid-ocean ridge: The MELT experiment, *Science*, **280**, 1215–1218.
- Gee, L.S. & Jordan, T.H., 1992. Generalised seismological data functionals, *Geophys. J. Int.*, **111**, 363–390.
- Grand, S.P., 2002. Mantle shear-wave tomography and the fate of subducted slabs, *Phil. Trans. R. Soc. Lond. A*, **360**, 2475–2491.
- Gu, Y.J., Dziewonski, A.M., Su, W.-J. & Ekström, G., 2001. Models of the mantle shear velocity and discontinuities in the pattern of lateral heterogeneities, *J. geophys. Res.*, **106**, 11 169–11 199.
- Káráson, H. & van der Hilst, R.D., 2000. Constraints on Mantle Convection from seismic tomography, in *The History and Dynamics of Global Plate Motions*, pp. 277–288, eds Richards, M.A., Gordon, R.G. & van der Hilst, R.D., AGU, Geophys. Monograph 121.
- Kennett, B.L.N., Engdahl, E.R. & Buland, R., 1995. Constraints on seismic velocities in the Earth from traveltimes, *Geophys. J. Int.*, **122**, 108–124.
- Komatitsch, D., Ritsema, J. & Tromp, J., 2002. The spectral-element method, beowulf computing, and global seismology, *Science*, **298**, 1737–1742.
- Laske, G. & Masters, G., 1996. Constraints on global phase velocity maps from long-period polarization data *J. geophys. Res.*, **101**, 16 059–16 075.
- Lebedev, S. & Nolet, G., 2003. Upper mantle beneath southeast Asia from S velocity tomography, *J. geophys. Res.*, **108**, doi:10.1029/2000JB000073.
- Lebedev, S., Chevrot, S. & van der Hilst, R.D., 2002. Seismic evidence for olivine phase changes at the 410- and 660-kilometer discontinuities, *Science*, **296**, 1300–1302.
- Lebedev, S., Chevrot, S. & van der Hilst, R.D., 2003. Correlation between the shear-speed structure and thickness of the mantle transition zone, *Phys. Earth planet. Inter.*, **136**, 25–40.
- Lebedev, S., Nolet, G., Meier, T. & van der Hilst, R.D., 2005. Automated multimode inversion of surface and S waveforms, *Geophys. J. Int.*, **162**, 951–964.
- Lebedev, S., Meier, T. & van der Hilst, R.D., 2006. Asthenospheric flow and origin of volcanism in the Baikal Rift area, *Earth planet. Sci. Lett.*, **249**, 415–424.
- Liu, H.-P., Anderson, D.L. & Kanamori, H., 1976. Velocity dispersion due to anelasticity: implications for seismology and mantle composition, *Geophys. J. R. astr. Soc.*, **47**, 41–58.
- Marquering, H., Snieder, R. & Nolet, G., 1996. Waveform inversions and the significance of surface-wave mode coupling, *Geophys. J. Int.*, **124**, 258–278.
- Marquering, H., Nolet, G. & Dahlen, F.A., 1998. Three-dimensional waveform sensitivity kernels, *Geophys. J. Int.*, **132**, 521–534.
- Masters, G., Johnson, S., Laske, G. & Bolton, H., 1996. A shear-velocity model of the mantle, *Phil. Trans. R. Soc. Lond. A*, **354**, 1385–1411.
- Masters, G., Laske, G., Bolton, H. & Dziewonski, A., 2000. The relative behavior of shear velocity, bulk sound speed, and compressional velocity in the mantle: implications for chemical and thermal structure, in *Earth’s Deep Interior*, eds Karato, S., Forte, A.M., Liebermann, R.C., Masters, G. & Stixrude, L., AGU Monograph 117, AGU, Washington, DC.
- Megnin, C. & Romanowicz, B., 2000. The three-dimensional shear velocity structure of the mantle from the inversion of body, surface and higher-mode waveforms, *J. geophys. Res.*, **143**, 709–728.
- Meier, T., Lebedev, S., Nolet, G. & Dahlen, F.A., 1997. Diffraction tomography using multimode surface waves, *J. geophys. Res.*, **82**, 8255–8267.

- Nolet, G., 1990. Partitioned waveform inversion and two-dimensional structure under the Network of Autonomously Recording Seismographs, *J. geophys. Res.*, **95**, 8499–8512.
- Ritsema, J., van Heijst, H.J. & Woodhouse, J.H., 2004. Global transition zone tomography, *J. geophys. Res.*, **109**, doi:10.1029/2003JB002610.
- Ritzwoller, M.H. & Levshin, A.L., 1998. Eurasian surface wave tomography: group velocities, *J. geophys. Res.*, **103**, 4839–4878.
- Shapiro, N.M. & Ritzwoller, M.H., 2002. Monte-Carlo inversion for a global shear-velocity model of the crust and upper mantle, *Geophys. J. Int.*, **151**, 88–105.
- Simons, F.J., van der Hilst, R.D., Montagner, J.-P. & Zielhuis, A., 2002. Multi-mode Rayleigh wave inversion for heterogeneity and azimuthal anisotropy of the Australian upper mantle, *Geophys. J. Int.*, **151**, 738–754.
- Sleep, N.H., 2003. Fate of mantle plume material trapped within a lithospheric catchment with reference to Brazil. *Geochem. Geophys. Geosys.*, **4**, doi:10.1029/2002GC000464.
- Su, W.-J., Woodward, R.L. & Dziewonski, A.M., 1994. Degree 12 model of shear velocity heterogeneity in the mantle, *J. geophys. Res.*, **99**, 6945–6980.
- Trampert, J. & Spetzler, J., 2006. Surface wave tomography: finite-frequency effects lost in the null space, *Geophys. J. Int.*, **164**, 394–400.
- Trampert, J. & Woodhouse, J.H., 1995. Global phase velocity maps of Love and Rayleigh waves between 40 and 150 s period, *Geophys. J. Int.*, **122**, 675–690.
- Qin, Y., Capdeville, Y., Maupin, V. & Montagner, J.-P., 2006. Synthetic Dataset To Benchmark Global Tomographic Methods, *EOS, Trans. Am. geophys. Un.*, **87**(46), 512, doi:10.1029/2006EO460004.
- Wang, Z. & Dahlen, F.A., 1995a. Spherical-spline parameterization of 3-dimensional earth models. *Geophys. Res. Lett.*, **22**, 3099–3102.
- Wang, Z. & Dahlen, F.A., 1995b. Validity of surface-wave ray theory on a laterally heterogeneous earth, *Geophys. J. Int.*, **123**, 757–773.
- Weeraratne, D.S., Forsyth, D.W., Fischer, K.M. & Nyblade, A.A., 2003. Evidence for an upper-mantle plume beneath the Tanzania Craton from Rayleigh wave tomography, *J. Geophys. Res.*, **108**(B9), 2427, doi:10.1029/2002JB002273.
- Wessel, P. & Smith, W.H.F., 1995. New version of the Generic Mapping Tools released, *EOS Trans. AGU*, **76**, 329.
- Woodhouse, J.H. & Dziewonski, A.M., 1984. Mapping the upper mantle: three-dimensional modeling of Earth structure by inversion of seismic waveforms, *J. geophys. Res.*, **89**, 5953–5986.
- Yoshizawa, K. & Kennett, B.L.N., 2002. Determination of the influence zone for surface wave paths, *Geophys. J. Int.*, **149**, 440–453.
- Zhang, Y.S. & Tanimoto, T., 1993. High-resolution global upper mantle structure and plate tectonics, *J. geophys. Res.*, **98**, 9793–9823.
- Zhang, X., Paulssen, H., Lebedev, S. & Meier, T., 2007. Surface wave tomography of the Gulf of California, *Geophys. Res. Lett.*, **34**, doi:10.1029/2007GL030631.
- Zhou, Y., Dahlen, F.A., Nolet, G. & Laske, G., 2005. Finite-frequency effects in global surface-wave tomography, *Geophys. J. Int.*, **163**, 1087–1111.
- Zhou, Y., Nolet, G. & Dahlen, F.A., 2006. Global upper-mantle structure from finite-frequency surface-wave tomography, *J. geophys. Res.*, **111**, doi:10.1029/2005JB003677.